

Cross-talk between topological defects in different fields revealed by nematic microfluidics

Luca Giomi^a, Žiga Kos^b, Miha Ravnik^{b,c}, and Anupam Sengupta^{d,e,1,2}

alnstituut-Lorentz for Theoretical Physics, Leiden University, 2333 CA Leiden, The Netherlands; ^bFaculty of Mathematics and Physics, University of Ljubljana, 1000 Ljubljana, Slovenia; ^cCondensed Matter Physics Department, Jožef Stefan Institute, 1000 Ljubljana, Slovenia; ^dInstitute for Environmental Engineering, Department of Civil, Environmental, and Geomatic Engineering, Eidgenössische Technische Hochschule (ETH) Zurich, 8093 Zurich, Switzerland; and ^eMax-Planck-Institute for Dynamics and Self-Organization, 37077 Goettingen, Germany

Edited by Tom C. Lubensky, University of Pennsylvania, Philadelphia, PA, and approved June 1, 2017 (received for review February 17, 2017)

Topological defects are singularities in material fields that play a vital role across a range of systems: from cosmic microwave background polarization to superconductors and biological materials. Although topological defects and their mutual interactions have been extensively studied, little is known about the interplay between defects in different fields-especially when they coevolve—within the same physical system. Here, using nematic microfluidics, we study the cross-talk of topological defects in two different material fields—the velocity field and the molecular orientational field. Specifically, we generate hydrodynamic stagnation points of different topological charges at the center of starshaped microfluidic junctions, which then interact with emergent topological defects in the orientational field of the nematic director. We combine experiments and analytical and numerical calculations to show that a hydrodynamic singularity of a given topological charge can nucleate a nematic defect of equal topological charge and corroborate this by creating -1, -2, and -3 topological defects in four-, six-, and eight-arm junctions. Our work is an attempt toward understanding materials that are governed by distinctly multifield topology, where disparate topology-carrying fields are coupled and concertedly determine the material properties and response.

multifield topology | nematic liquid crystals | topological defects | microfluidics | cross-interactions

efects are ubiquitous in nature and are at the heart of numerous physical mechanisms, including melting in 2D crystals (1), cosmic strings (2), and other topological defects in the early universe (3). Vortices are possibly the most common examples of defects in flowing media (4, 5). In a typical hydrodynamic vortex, the fluid velocity, ν , rotates by 2π along any closed loop around the vortex core and has an undefined direction at the core. More generally, topological defects are singular points or lines in a distinct scalar, vector, or tensor field that can be characterized by topological invariants, including winding number (or index) for 2D, and topological charge for 3D variations of the fields (6, 7). Topological defects have been long known to mediate key processes in a wide range of settings, including knotted flow field stream lines (8), defects in light fields (9), knotted defect lines in complex fluids (10), defects in type 2 superconductors (11), spontaneous flow in active fluids (12–15), and even, conduction properties of electron nematics (16).

The interaction between topological defects is governed by the defect topology and the underlying energetics. Similar to electrically charged particles, like-sign topological defects, in general, repel each other, whereas defects of opposite sign attract. However, this interaction can be additionally affected by the geometry and surface properties of the environment (17, 18) and the presence of an external stimulus (19–23). Emergence of topological defects in a field and the resulting interactions between them have been well-characterized (24). However, how topological defects in a system can coevolve in and interact across disparate fields is largely unexplored. It is rather recent that multi-

field topological interactions were shown in optics, where singularities in optical birefringence created topological defects in the light field (25, 26). The growing evidence that topological defects perform vital biological functions (27–29) creates a fundamental need for an integrated understanding of defect interactions, especially in relation to those in a different field (for instance, in the surrounding microenvironment).

Complex nematic fluids have proven to be a versatile test bed for studying, testing, and realizing diverse topological concepts (30-32), owing primarily to their inherent softness and strong response to external stimuli and in context of this work, their material fluidity (33, 34). Liquid crystal microfluidics (35) has emerged as a potent toolkit to modulate fluid and material structures caused by the coupling between the two main material fields-the fluid velocity field and the molecular orientational field (director) (34). The flow director coupling regulates transport properties of nematic suspensions (36, 37), tunes the rheology of the liquid crystals (LCs) (38–41), and mediates annihilation-creation dynamics of topological defects (21, 42). Microfluidics based on complex anisotropic fluids has allowed for potential applications (43) and novel designs of microcargo transport (44), tunable fluid resistivity (45), color filters (46), and biochemical sensors (47).

In this paper, we study the emergence of topological defects in two different fields present in the nematic microfluidic system: the stagnation point, a hydrodynamic singularity in the

Significance

Topological defects play a defining role in systems as extensive as the universe and as minuscule as a microbial colony. Despite significant advances in our understanding of topological defects and their mutual interactions, little is known about the formation and dynamics of defects across different material fields embedded within the same system. Here, using nematic microfluidics as a test bed, we report how topological defects in the flow and the orientational fields emerge and cross-talk with each other. Although discussed in a nematofluidic context, such multifield topological interactions have potential ramifications in a range of systems spanning vastly different length and time scales: from material designing, to exploration of open questions in cosmology and living matter.

Author contributions: L.G., M.R., and A.S. designed research; L.G. developed particle model and performed analytical calculations; Ž.K. and M.R. performed numerical simulations; A.S. conceptualized research, conducted experiments, analyzed data, and provided advice for all parts of the work; and L.G., Ž.K., M.R., and A.S. wrote the paper.

The authors declare no conflict of interest.

This article is a PNAS Direct Submission.

¹Present address: Institute for Environmental Engineering, Eidgenössische Technische Hochschule (ETH) Zurich, 8093 Zurich, Switzerland.

²To whom correspondence should be addressed. Email: anupams@ethz.ch.

This article contains supporting information online at www.pnas.org/lookup/suppl/doi:10. 1073/pnas.1702777114/-/DCSupplemental.

flow velocity field, and the nematic defect, a topological singularity in the molecular orientation field. We characterize the cross-interaction between these topological defects using starshaped microfluidic junctions and flowing nematic fluid (Fig. 1A). We show that the nucleation and the nature of the nematic defects are determined by the topology of the flow defect, such that a hydrodynamic stagnation point of topological charge 1 - N/2, with N as the number of arms of the junction, nucleates a defect of the same topological charge in the nematic director field. The multifield defect interaction is underpinned by a coupling between the two fields, which we tune via microfluidic geometry, and the nematic flow parameters. We observe transformations between topological states, including the decay of nematic defects to lower topological charges. Notably, the reconfiguration timescales for the defects from the two different fields— 10^{-5} s for the hydrodynamic stagnation points and ~ 1 s for the nematic defects—are resolved, and possible ramifications of this separation of timescales are discussed. Finally, this work is a realization of a material system governed by the topology of multiple coupled fields—a platform that can be extended further, potentially leading to the development of interesting topological materials or topological material phenomena.

Tuning Topology with Hydrodynamics

We study the emergence of topological defects using a combination of experiments, numerical modeling, and theory. Experimentally, we use star-shaped microfluidic junctions fabricated by soft lithography techniques (Materials and Methods and SI *Text*). Our experimental results are complemented by theoretical analysis and numerical modeling based on Beris-Edwards-type approach—a powerful tool to study nematic structures, especially defects at mesoscopic scale (34).

The cross-interaction between the velocity and the nematic fields is governed by an interplay of multiple effects: material viscosity, nematic elasticity, channel dimensions, and the strength of the flow (Fig. 1A). The combined effect is captured by a single dimensionless number, the Ericksen number, $Er = \eta v l / K$ (48), with η being the effective viscosity, v being the flow velocity, lbeing the channel hydraulic diameter, and K being the 4'-pentyl-4-biphenylcarbo-nitrile (5CB) elastic constant (SI Text). The Ericksen number $(0.4 \lesssim \text{Er} \lesssim 70 \text{ in our experiments})$ thus gives a relative measure of the viscous and elastic stresses.

Fig. 1B shows the nematic defects obtained in four-, six-, and eight-arm microfluidic junctions. In each case, no defect was observed for Er < 1—a nematofluidic regime in which the elastic torque far outweighs the viscous torque. In the four-arm junction, the first appearance of a -1 defect is observed at Er = 2and found to stabilize at Er > 5. Fig. 1B, Top (imaged at Er \approx 10) shows polarization optical micrograph (POM) of a stable defect of strength -1 at the center of the junction. Increasing the number of arms (Fig. 1B, Middle and Bottom) results in increase in the net topological charge at the junction center: -2 (imaged at ${\rm Er} \approx 18$ in the six-arm channel) and -3 (imaged at ${\rm Er} \approx 22$ in the eight-arm channel). High charge defects decayed into multiples of the -1 defects: the -2 defect decayed into a pair of -1 defects, and the -3 defect decayed into three -1 defects (see Fig. S1). By overlaying the positions of the hydrodynamic and nematic topological defects, we find that, in a four-arm

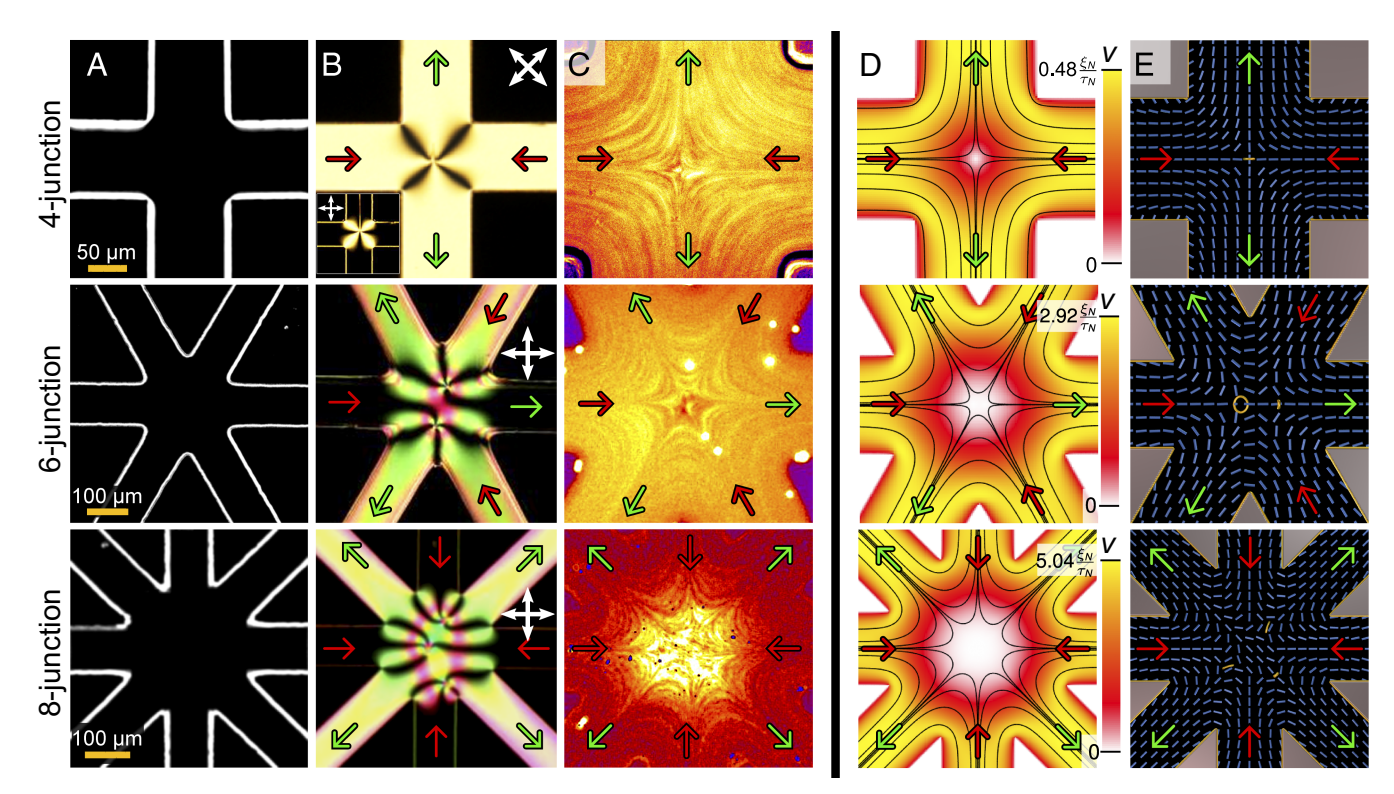


Fig. 1. Emergence of nematic topological defects and hydrodynamic singularities at a microfluidic junction. (A) Generic star-shaped microfluidic junctions. Four-, six-, and eight-arm microfluidic junctions and (B) corresponding POM images of the emergent topological defects at the center: -1 (four-arm junction), -2 defect split into two -1 defects (six-arm junction), and -3 defect split into three -1 defects (eight-arm junction). The double-headed arrows indicate the orientation of the crossed polarizers. The inflow and outflow arms are indicated by the red and green arrows, respectively. (C) Epifluorescent imaging of flowing fluorescent tracers reveals the hydrodynamic stagnation points at the geometric centers of each microfluidic junction. (D and E) Nematic flows at microfluidic junctions reproduced in numerical simulations. (D) Streamlines of flow profile in simulations. The range in which the velocity magnitude is drawn is given in units of nematic correlation length, ξ_N , divided by the characteristic nematic timescale, τ_N (SI Text). (E) The director profile (blue rods) and the isosurface of the nematic scalar-order parameter, drawn at S = 0.4 in yellow, as corresponding to the flow field in D.

junction, the -1 defect is within a micrometer from stagnation point. When averaged over time, the positions of the topological defects coincided. Similarly, in the six- and eight-arm junctions, the defects of higher charge (existing as multiples of -1 defect) are found to fall within a stagnation zone, a region at the junction center where the flow speed was less than 10% of the far field value.

We have reproduced the experimental results in silico using numerical simulations of 3D microfluidic junctions based on the Navier-Stokes equation coupled with the Beris-Edwards equations of nematodynamics (49) (Materials and Methods and SI *Text*). Fig. 1 D and E shows the numerical flow velocity and the nematic ordering at the four-, six-, and eight-arm junctions. The isosurfaces of the nematic order parameter (Fig. 1E) show stable -1 defect loops (i.e., defects of charge -1 consisting of a disclination loop with half-integer winding number), in good qualitative agreement with the experimental results. The numerical modeling shows that the material flow singularity emerges as a line region, extending from the top to the bottom of the channel, whereas the nematic defects evolve into small loops, which are topologically equivalent to 3D point defects (32). However, from a topological perspective, our setup allows us to fully characterize the 3D nematic defects by an effective 2D invariant, like the winding number. In essence, by simply capturing the midplane intersection of the nematic field, we are able to describe the nematic defect, because the channel geometry and the anchoring conditions limit any possible variation of the director field normal to the midplane (50). To generalize, the demonstrated system gives the cross-interaction between topological line defects and point defects (which at topological level, can be considered with 2D invariants), creating an interesting topological test bed with defects of different dimensionality.

Global Constraints and Local Forces

The emergent topological structure of the defects at the junction center results from a combination of global topological constraints and local mechanical effects. For the analytical treatment that follows, we consider the channel midplane only and a 2D nematic field within this plane. Because flow tends to align the director along the channel, a generic junction with 2narms yields 2n nematic defects at the corners of the polygon shown in Fig. 2A, Upper, each with winding number +1/2 (2D) topological charge). The total topological charge of the nematic field in the midplane of the junction, however, is constrained by the Poincaré-Hopf theorem (51), by virtue of which a compensatory charge, $k_{\text{bulk}} = 1 - n$, emerges in the bulk of the junction. Effectively, the homeotropic boundary conditions within the junction region are equivalent to a circle with perpendicular director orientation. Thus, in the case of a four-arm junction, $k_{\text{corners}} = 2$, and $k_{\text{bulk}} = -1$. For a six-arm junction, however, $k_{\text{corners}} = 3$, $k_{\text{bulk}} = -2$, and so on. At large Ericksen numbers, the director is flow-aligned, and the negative topological charge, at the expense of the system elastic energy, is attracted toward the central stagnation point (Figs. S2 and S3). To allow for analytic calculation of the basic cross-interaction between the flow and nematic defects, the considered microfluidic geometry is simplified to a 2D midplane of the channel, where the nematic director is written as a 2D field, $\mathbf{n} = (\cos \theta, \sin \theta, 0)$. The dynamics of the angle θ is governed by the following partial differential equation

$$(\partial_t + \mathbf{v} \cdot \nabla)\theta = \frac{K}{\gamma} \nabla^2 \theta + \omega_{xy} - \lambda (u_{xx} \sin 2\theta - u_{xy} \cos 2\theta).$$

where \mathbf{v} is the flow velocity; $\omega_{ij} = (\partial_i v_j - \partial_j v_i)/2$ and $u_{ij} = (\partial_i v_j + \partial_j v_i)/2$ are the vorticity and strain rate tensor, respectively; and γ is the rotational viscosity. The constant λ is the flow alignment parameter, which determines the director reori-

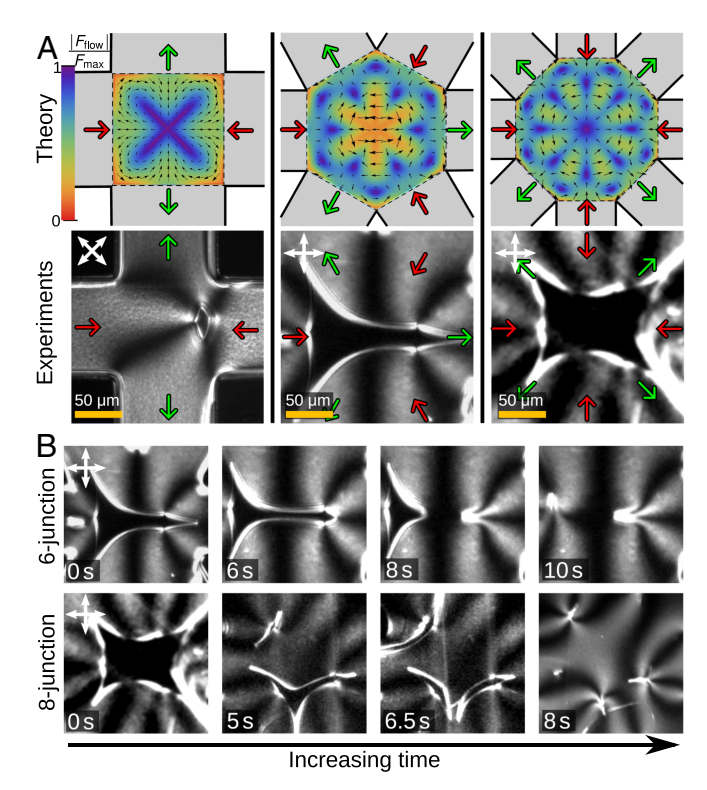


Fig. 2. Fractionalization of topological defects. (*A, Upper*) The hydrodynamic force field experienced by a 2D defect of charges -1, -2, and -3 confined inside four-, six-, and eight-arm junctions. *A, Lower* shows POM images of nematic defects right after formation: -1 defect loop at the four-arm junction, -2 defect at the six-arm junction, and -3 defect at the eight-arm junction. In each case, the defect loop encloses a homeotropic domain, close to the junction center, where the surface-induced anchoring remains unperturbed. Outside this domain, the nematic director is aligned because of the flow. (*B*) The higher-strength topological defects decay into multiple defects of charge -1, shown here as a time sequence for (*Upper*) -2 and (*Lower*) -3 defect. The -1 loop defect stabilizes by shrinking the enclosed homeotropic domain and thereby, reducing the effective length of the defect loop (Fig. 3*A*).

entation in response to a shear flow (34, 48). For 5CB used in our experiments, $\lambda \approx 1.1$, and the director orients at an angle $\Delta\theta \approx 13^\circ$ with respect to the flow (52). Owing to the symmetry of the junction geometry, the flow, in proximity of the central stagnation point, is irrotational. In polar coordinates (r,ϕ) , with r=0 being the junction center, an analytical approximation yields $v_r=v_0(r/\mathcal{R})^{n-1}\cos n\phi$ and $v_\phi=-v_0(r/\mathcal{R})^{n-1}\sin n\phi$, with v_0 being the flow speed at the center of the channels and \mathcal{R} being a length scale proportional to the channel width (SI Text). Consequently, for a perfectly flow-aligning system $(\lambda=1)$, the ideal defective configuration $\theta=(1-n)\phi$ is an exact solution of Eq. 1 (SI Text). For $\lambda\gtrsim 1$, the solution departs from this ideal form but however, still preserves the rotational symmetry.

Whereas emergence of the equilibrium singular director field depends exclusively on the symmetry of the flow in proximity of the stagnation point, its stability depends on the flow structure over the entire junction. We clarify this using an effective particle model for the dynamics of defects in the presence of a generic potential energy field that originates from a background flow at sufficiently large Ericksen numbers. Let us consider the generic free energy $\mathscr{F} = \int dA[K|\nabla\theta|^2/2 + U(\theta)]$, where $U(\theta)$ is a potential energy density caused by the interaction with an externally imposed flow, and that the system comprises a given number of topological defects of topological charge k_i at positions $\mathbf{R}_i = (X_i, Y_i)$. Extending a classic approach by Kawasaki (53)

and Denniston (54), one can then construct an equation of motion for the moving defect as (SI Text)

$$\dot{\mathbf{R}}_i = \mathbf{v}(\mathbf{R}_i) + \mu_i \left(2\pi K \sum_{j \neq i} k_i k_j \frac{\mathbf{R}_i - \mathbf{R}_j}{|\mathbf{R}_i - \mathbf{R}_j|^2} + \mathbf{F}_i \right), \quad [2]$$

where $\mu_i \sim 1/(\gamma k_i^2)$ is a mobility coefficient. The second term on the right-hand side of Eq. 2 corresponds to the wellknown Coulomb-like elastic interaction between the topological charges, whereas the third term, given by $F_i = -\nabla_{R_i} \int dA \ U(\theta)$, represents the force experienced by a defect moving in a potential energy field. In the presence of hydrodynamic flow, the latter can be calculated as (SI Text)

$$\boldsymbol{F}_{i} = k_{i} \int dA \frac{\hat{\boldsymbol{z}} \times (\boldsymbol{r} - \boldsymbol{R}_{i})}{|\boldsymbol{r} - \boldsymbol{R}_{i}|^{2}} \left[\omega_{xy} - \lambda (u_{xx} \sin 2\theta - u_{xy} \cos 2\theta) \right],$$
[3]

where θ is approximated as a linear superposition of the local orientations associated with all of the defects [i.e., $\theta(\mathbf{r}) \approx$ $\sum_{j} k_{j} \arctan(y - Y_{j})/(x - X_{j})$]. Fig. 2A shows the force field, calculated from Eq. 3 (normalized by the maximal force value), experienced by disclinations of topological charges -1, -2, and -3 placed within the respective junctions. The corresponding flow field, given by the tensorial elements u_{ij} and ω_{ij} in Eq. 3, has been analytically estimated, taking into account the rotational symmetry and the relative position of the stagnation point at the junction (SI Text). Consistent with our experimental and numerical results in 3D geometry of the channels, we found that defects of topological charge k < 0, analytically considered in 2D geometry, experience an effective attractive force toward a central stagnation point having the same negative topological charge. Such a force causes the defects to move toward the center of the junction, forming a stable equilibrium configuration. The positive defects, however, are subject to a repelling force that pushes them out of the junction center (SI Text), thus protecting the internal negative defects from annihilation.

Charge Fractionalization and Defects Unbinding

Defects having large negative topological charge (i.e., k < -1) are prone to decay into multiples of -1 defects. We have experimentally resolved the dynamics of the collapse of the defect loop at the central junction. Fig. 2A, Lower shows POMs of the defect loops immediately after their formation. At the center of the four-arm junction, we observe a defect loop of charge -1 (Fig. 2A, Lower Left), which within a short time, stabilizes into a -1 monopole of the pseudoplanar texture (50) (Movie S1). The defects in the six- and eight-arm junctions emerge as loops of charges -2 and -3, respectively (Fig. 2A, Lower Center and Lower Right), and gradually decay into multiple -1 charged defects (Fig. 2B). As presented in Fig. 2B, Upper, the -2 loop fractionalizes into two smaller -1 loops, and within 10 s, stabilized into a pair of -1defects. The fractionalization of the $-3 \log (\text{Fig. } 2B, Lower)$ proceeds in three steps. (i) A loop of charge -3 splits into a -2 loop and a -1 loop. (ii) The -1 loop shrinks, while the -2 loop splits into two -1 loops. (iii) Finally, all three -1 defect loops shrink down to the -1 structure, completing the fractionalization process. These emergent -1 defects are singularities of the pseudoplanar texture, with positions that are stable over time. However, their relative arrangement can be changed by tuning the flow within arms of the junction (*SI Text* and Fig. S1).

The behavior described above results from two competing effects. On the one hand, the hydrodynamic forces tend to concentrate the negative topological charge at the center of the junction. On the other hand, the elastic forces drive the repulsion of likesign defects. This effect of elasticity favors the fractionalization of a central k = -n topological charge into n defects of charge -1. Furthermore, hydrodynamic stagnation points of charge -2 and -3 (Fig. 1C) are susceptible to decay and can become unstable with respect to any perturbation of the pressure distribution across the channels. A slight asymmetry in the pressure distribution causes the central stagnation point to split into multiples of stagnation points of charge -1, thus further favoring the unbinding of defects.

Dynamics of Defect Nucleation in a Four-Arm Junction

The higher stability of a -1 defect relative to the -2 (or -3) defect allows for the analysis of the defect nucleation in our

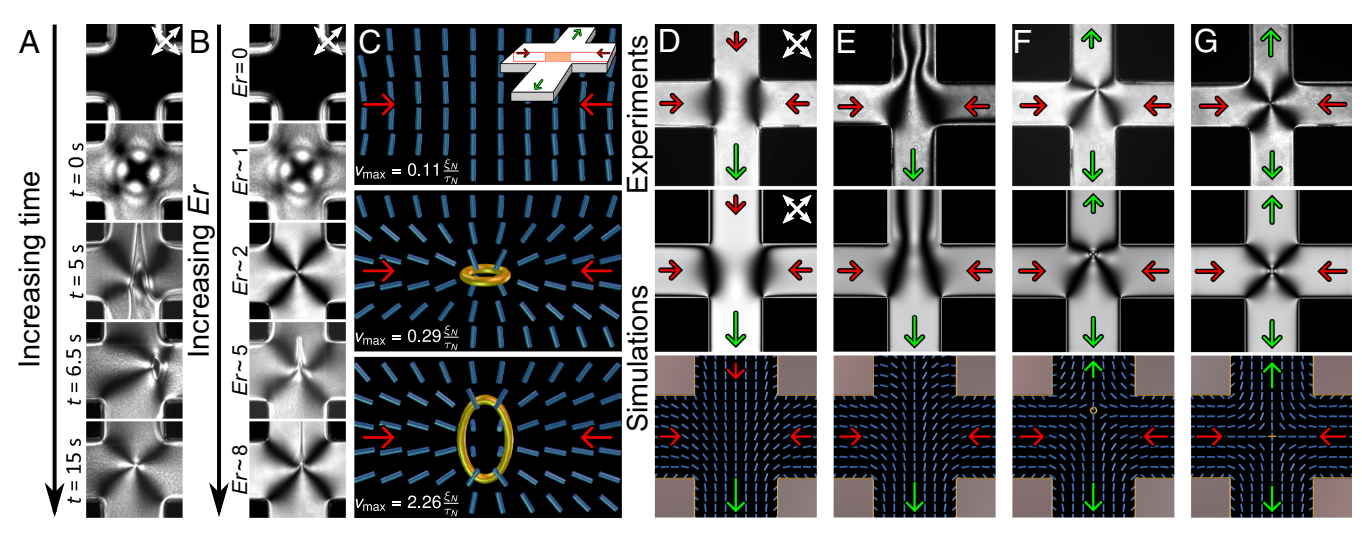


Fig. 3. Dynamics of defect nucleation in a four-arm junction. (A) Emergence of -1 defect over time at the four-arm junction visualized as POM image (Er = 8). (B) Polarization micrographs of the nematic flow texture show the transition from a defect-free state to a -1 topological defect at the junction (Er \approx 2). The defect can stretch at higher Er, shown here at Er \gtrsim 5. (C) Numerically simulated nematic director field with increasing Er within the plane indicated in *Inset*; director is shown in blue, and defects are shown as isosurfaces of nematic degree of order S = 0.4. (D and E) Continuous defect-free director field observed in specific inflow-outflow combinations in experiments (Top) and confirmed in simulations (Middle and Bottom). (F and G) When symmetrical flow conditions are restored (each inflow arm is flanked by two outflow arms), a -1 defect emerges and stabilizes at the geometric center of the four-arm junction when the flow speeds in all of the arms are equal (G).

microfluidic experiments. Fig. 3A shows creation of the -1nematic defect loop at the stagnation point, when flow through the two facing inlet arms meets simultaneously at the four-arm junction (Er = 8). On starting the flow synchronously in a 5CBfilled four-arm microfluidic device, the director field aligns along the flow direction. The alignment initiates close to the respective inlets of the opposite-facing arms; however, farther downstream, the director field remains relatively undisturbed. Thus, each inlet arm develops two director domains: upstream, a flow-aligned director domain, and downstream, an unperturbed homeotropic domain. These two director domains are separated by a disclination line with half-integer winding number (41, 52). The disclination travels downstream in each of the facing inflow arms (Fig. S4 and Movie S2) and meets head on at the junction center (Fig. 3A, row 3). On meeting, the singular disclinations merge into a defect loop, enclosing a homeotropic domain (Fig. 3A, row 4), which gradually shrinks and finally stabilizes into a -1 defect at the junction center (SI Text and Movie S1). We would like to emphasize that homeotropic anchoring, in absence of flow, supports multiple director configurations. These energetically stable or metastable configurations emerge because of an interplay between the cross-section geometry (rectangular, square, or circular), anchoring strength, and the curvature (or sharpness) of the channel corners (35, 41) and set the initial conditions for our flow experiments.

In a second approach, we have gradually increased the flow speed (in steps of Er=0.5) in each inflow arm and allowed the director field to equilibrate before increasing Er further. The exact structure of the nematic field and the emergence of the nematic topological defects are observed to be strongly dependent on the Ericksen number, which we vary by changing the magnitude of the flow field. Fig. 3B presents a sequence of polarized micrographs of the nematic texture at the junction center. The first appearance of the -1 defect loop was recorded at $Er \approx 2$. At higher Er, the -1 defect loop was located stably at the center; however, it could extend along one or either side of the outflow arms (Fig. 3B, rows 4 and 5). The profile of the

director within the four-arm junction is obtained by using numerical modeling (Fig. 3C). Increasing the flow speed (or Er) results in a further pronounced flow alignment of the director, and at still larger Er values, the system attains a complete flow alignment with the nematic director aligned roughly parallel to the channel direction. Because the two flow-aligned domains meet at the junction center, the mismatch in the nematic director leads to the formation of a small defective loop of charge -1 (Fig. 3C, Middle). At high Er values, the flow shear takes over the elastic forces and determines the director field in the proximity of the newly emerged nematic defect (35). The defect loop can also flip and stretch out of the vertical plane (Fig. 3C, Bottom). A stable -1 defect loop can also emerge by designing a specific modulation of the flow at the four-arm junction. As shown in Fig. 3D, a combination of three inflow arms (left, right, and top) and one outflow arm (bottom), results in a defect-free state at the junction center. By switching off the inflow in the top arm (Fig. 3E), the system gradually reorganizes, and as symmetric outflow conditions are restored, a transition to the defective configuration (Fig. 3 F and G) is observed. This result shows that designing different microfluidic circuits and junction geometries could be used as an interesting route for creation of nematic defect structures of various complexity.

Discussion

The coupling between the velocity and the orientational fields serves as a tunable mechanism for designing multifield topology in nematic microfluidic systems. Our results reveal that this coupling also underpins the cross-interaction between the topological defects in the flow velocity and the nematic orientational fields. We quantify the interaction strength between the hydrodynamic and nematic defects in a four-arm junction by perturbing the defects out of their equilibrium position and analyzing the relative separation between them over time. Altering the inlet pressure in one of the flow arms displaces the stagnation point off the center first followed by gradual recovery of the nematic director. Fig. 4 *A* and *C* presents this dynamics using numerical

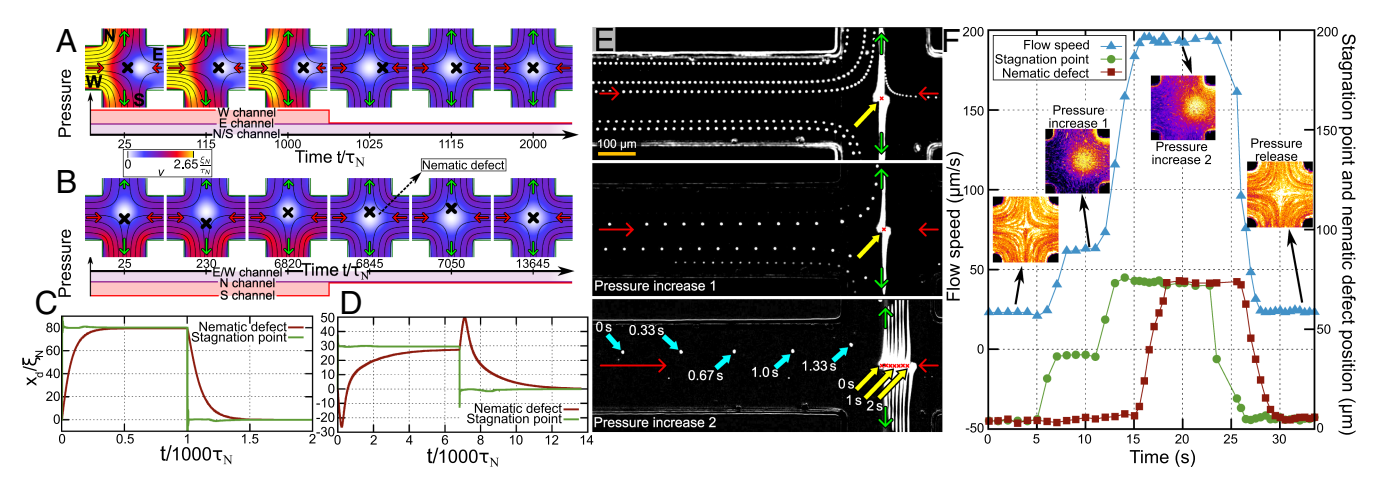


Fig. 4. Cross-talk between topological defects in different fields. (A) Simulations show displacement of the nematic defect and the hydrodynamic stagnation point when pressure in the left arm (W) of device was increased. The stagnation point shifts to a new position followed by a much slower shift of the nematic defect. Before the pressure pulse is turned off (column 3), the stagnation point and the nematic defect are completely realigned. After the pressure is released, the stagnation point shifts back to the original position, slowly followed by the nematic defect. The exact position of the stagnation point and the nematic defect over time is shown in C. (B) When pressure in the bottom arm is decreased, the nematic defect first drifts away from the shifted stagnation point (i.e., against the flow). At longer times, the nematic defect approaches the stagnation point, and finally, they overlay (D). (E) Positions of the hydrodynamic stagnation point and the nematic defect are measured experimentally as functions of time. White dots show the transport of tracer particles over time, and the yellow arrows indicate the position of the nematic defect center. F, Insets show the corresponding positions of the hydrodynamic stagnation point over time obtained from the fluorescence measurements of the tracer particle flow at the junction center. (F) The increased pressure pulse in experiments confirms numerical results: the stagnation point first undergoes an instantaneous shift, and then, the nematic defect drifts toward the stagnation point. On releasing the pressure, the defects return back to their initial position, starting with the stagnation point and then followed by the nematic defect.

calculations dynamics. After the stagnation point and the nematic defect are separated (Fig. 4A, column 1), the latter approaches the stagnation point, and within $1,000\tau_N$, the stagnation point and the nematic defect coincide again. Altering the pressure in an outflow arm also shifts the stagnation point first followed by recovery of the -1 defect (Fig. 4 B and D). However, because the nematic defect now moves against the flow, the recovery is 10 times slower than in the previous case. Furthermore, the nematic defect initially moves backward before progressing toward the hydrodynamic stagnation point at the new

Experimentally, we perturb our system out of the equilibrium state by marginally increasing the inlet pressure in the left arm (Fig. 4E) and record the position of the defects over time. By overlaying consecutive frames of the recorded video data, we obtain a processed micrograph that captures the transport of tracer particles (bright dots along the flow direction in Fig. 4E) and the position of the defect over time (indicated by the yellow arrows in Fig. 4E). The separation between bright dots is the distance traveled by a particle over the time interval between consecutive frames. This recorded dynamics gives us a flow speed of 24 μm/s under equilibrium conditions as shown in Fig. 4E, Top. The topological defects remain colocalized at the center of the junction (no relative shift) (0-5 s in Fig. 4F). When we increase the inlet pressure in the left arm (Fig. 4E, Middle), the flow speed increases to $\approx 62 \mu \text{m/s}$ and shifts the stagnation point (pressure increase $1 \approx 15$ kPa) (Fig. 4F) by ≈ 40 µm to the right. The -1 nematic defect, however, remains locked at the center of the junction. Only on increasing the pressure further (v = 180μm/s) does the nematic defect shift. As shown in Fig. 4E, Bottom, the defect shifted by $\approx 90 \mu m$ before finally coinciding with the stagnation point at the new equilibrium position (pressure increase $2 \approx 50$ kPa) (Fig. 4F). When the perturbing pressure was released, the stagnation point rapidly returned to the junction center followed slowly by the -1 defect (pressure release in Fig. 4F). The observed dynamics shows a complex interaction between the hydrodynamic stagnation point and the nematic defect, which is clearly dependent on the direction of motion of the nematic defect relative to the local material flow. More generally and in a mechanics-motivated view, the emergent dynamics of the two defect types in the vicinity of each other could be viewed as induced by an interdefect force (or potential) that stems from the coupling of the two material fields and is inherently mediated by the topology (i.e., the topological charge) of the involved defects.

The cross-interaction between topological defects originating from different fields, although shown in the context of nematic microfluidics, is a phenomenon, which owing to its topological nature, is much more general in appeal. The demonstrated crosstalk relies on the existence of multiple spatially overlying material fields—in our case, vector type but it could also be scalar or tensorial—that are mutually coupled by some force-, stress-, or energy-like cross-coupling mechanism. Therefore, the natural candidates for such phenomena will be systems with pronounced transport effects or strongly interacting fields. As possibly the most far-reaching question of this type, such concepts of cross-field interacting defects could offer a physical framework for addressing phenomena in other areas of condensed matter physics, field theory, and cosmology.

In conclusion, the interplay between fluid flow and molecular orientation in nematic microfluidics has revealed that a hydrodynamic stagnation point can nucleate defects, whose topological charge can be hierarchically tuned by changing the rotational symmetry of the junction (Fig. S5 and SI Text) Importantly, our experiments, numerical modeling, and analytical calculations show that topological defects in different material fields crosstalk and that their characterization reveals a topology-dependent interaction between these defects of hydrodynamic and nematicordering origin. As defects from different fields can coexist in several soft and living matter systems, this work introduces an exciting perspective, and paves the way toward understanding the potential role of multifield topology in equilibrium and nonequilibrium systems.

Materials and Methods

Experimental Setup. We have used 5CB, a single-component nematic LC (18 $^{\circ}$ C < T < 33 $^{\circ}$ C) for experiments. The microfluidic channels had rectangular cross-section, with depth $d \approx 10~\mu\text{m}$, width $w = 100~\mu\text{m}$, and 15 mm length (unless otherwise specified). The channels were treated with 0.1% wt/wt aqueous solution of silane octadecyldimethyl(3-trimethoxysilylpropyl)ammonium chloride to create homeotropic surface anchoring (35). Before flow experiments, microchannels were filled with 5CB in its isotropic phase. After cooled down to the nematic phase, we have gradually increased the flow rate until topological defects emerged at the channel junction. The flow rate was varied between 0.01 and 2.0 μ L/h (corresponding flow speed, v, ranged between $2\mu m/s$ and $0.40 \, mm/s$) in each arm. Thus, the characteristic Reynolds number $\mathrm{Re} = \rho \mathrm{vI}/\eta$ ranged between 10^{-6} and 10^{-4} . Here, $\eta = 50 \,\mathrm{mPa}\,\mathrm{s}$ and $\rho = 1,025 \,\mathrm{kg/m^3}$ are the dynamic viscosity and density of 5CB, respectively, and $I = 4wd/2(w+d) \approx 18 \, \mu \text{m}$ is the hydraulic diameter of the rectangular microchannels. The corresponding Ericksen number $Er = \eta v I/K$, with K = 5.5 pN being the 5CB elastic constant (one-constant approximation), varied between 0.3 and 65.

Numerical Simulations. Our numerical simulations rely on Beris-Edwards formulation of nematodynamics (49) describing the evolution of system density, velocity, and nematic tensor order parameter by the coupled continuity equation, Navier-Stokes equation, and Beris-Edwards equation. Coupling between flow and orientational order is included by the nematic stress tensor and the flow-driven deformations of the nematic tensor order parameter profile that compete with the relaxation of nematic orientation toward the free energy minimum. The nematic free energy is constructed phenomenologically, including terms describing phase behavior, effective elasticity, and surface anchoring (34). Continuity and Navier-Stokes equations are solved numerically by a lattice Boltzmann algorithm (55), with open boundaries and pressure-driven flows through the channels. Simultaneously, evolution of nematic tensor order parameter is solved by a finite difference algorithm (SI Text).

ACKNOWLEDGMENTS. The authors thank Simon Čopar for insightful discussions on the dynamics of defect nucleation. A.S. thanks Stephan Herminghaus and Christian Bahr for discussions at different stages of this work. L.G. is supported by The Netherlands Organization for Scientific Research. Ž.K. and M.R. are supported by the Slovenian Research Agency Grants J1-7300, L1-8135, and P1-0099 and US Air Force Office of Scientific Research, European Office of Aerospace Research and Development Grant FA9550-15-1-0418, Contract 15IOE028. A.S. thanks Human Frontier Science Program Cross Disciplinary Fellowship LT000993/2014-C for support and the Max Planck Society for funding the initial phase of this work at the Max Planck Institute for Dynamics and Self-Organization, Goettingen, Germany.

- 1. Nelson DR, Halperin BI (1979) Dislocation-mediated melting in two dimensions. Phys Rev B 19:2457-2484
- 2. Ade PAR, et al. (2014) Planck 2013 results. XXV. Searches for cosmic strings and other topological defects. Astron Astrophys 571:A25.
- 3. Kibble TWB (1976) Topology of cosmic domains and strings. J Phys Math Gen 9:1387-
- 4. Newton I (1713) Philosophiæ Naturalis Principia Mathematica: General Scholium. Available at www.qutenberg.org/ebooks/28233?msg=welcome_stranger. Accessed June 27, 2017.
- 5. Batchelor GK (1967) Introduction to Fluid Dynamics (Cambridge Univ Press, Cambridge, UK).
- 6. Alexander GP, Chen BG, Matsumoto EA, Kamien RD (2012) Colloquium: Disclination loops, point defects, and all that in nematic liquid crystals. Rev Mod Phys 84:
- 7. Mermin ND (1979) The topological theory of defects in ordered media. Rev Mod Phys 51:591-648
- 8. Kleckner D, Irvine WTM (2013) Creation and dynamics of knotted vortices. Nat Phys 9:253-258.
- 9. Desyatnikov AS, Buccoliero D, Dennis MR, Kivshar YS (2012) Spontaneous knotting of self-trapped waves. Sci Rep 2:771.
- 10. Tkalec U. Raynik M. Čopar S. Žumer S. Muševič I (2011) Reconfigurable knots and links in chiral nematic colloids. Science 333:62-65

- 11. Tinkham M (1996) Introduction to Superconductivity (Dover Publications, Mineola,
- 12. Sanchez T, Chen DTN, DeCamp SJ, Heymann M, Dogic Z (2012) Spontaneous motion in hierarchically assembled active matter. Nature 491:431-434.
- 13. Giomi L, Bowick MJ, Mishra P, Sknepnek R, Marchetti MC (2014) Defect dynamics in active nematics. Philos Trans A Math Phys Eng Sci 372:20130365.
- 14. Keber FC, et al. (2014) Topology and dynamics of active nematic vesicles. Science 345:1135-1139
- 15. Giomi L (2015) Geometry and topology of turbulence in active nematics. Phys Rev X 5:031003.
- 16. Carlson EW, Dahmen KA (2011) Using disorder to detect locally ordered electron nematics via hysteresis. Nat Commun 2:379.
- 17. Sharifi-Mood N, Liu IB, Stebe KJ (2015) Curvature capillary migration of microspheres. Soft Matter 11:6768-6779.
- 18. Wei WS, et al. (2016) Dynamics of ordered colloidal particle monolayers at nematic liquid crystal interfaces. Soft Matter 12:4715-4724.
- Chuang I, Durrer R, Turok N, Yurke B (1991) Cosmology in the laboratory: Defect dynamics in liquid crystals. Science 251:1336-1342.
- 20. Tóth G, Denniston C, Yeomans JM (2002) Hydrodynamics of topological defects in nematic liquid crystals. Phys Rev Lett 88:105504
- 21. Giomi L, Bowick MJ, Ma X, Marchetti MC (2013) Defect annihilation and proliferation in active nematics. Phys Rev Lett 110:228101.
- 22. Bowick MJ, Giomi L, Shin H, Thomas CK (2008) Bubble-raft model for a paraboloidal crystal. Phys Rev E 77:021602.
- 23. Dierking I, et al. (2012) Anisotropy in the annihilation dynamics of umbilic defects in nematic liquid crystals. Phys Rev E 85:021703.
- 24. Chaikin PM, Lubensky TC (2005) Principles of Condensed Matter Physics (Cambridge Univ Press, Cambridge, UK).
- 25. Brasselet E (2012) Tunable optical vortex arrays from a single nematic topological defect. Phys Rev Lett 108:087801.
- Čančula M, Ravnik M, Žumer S (2014) Generation of vector beams with liquid crystal disclination lines. Phys Rev E 90:022503.
- 27. Peng C, Turiv T, Guo Y, Wei QH, Lavrentovich OD (2016) Command of active matter by topological defects and patterns. Science 354:882-885.
- Saw TB, et al. (2017) Topological defects in epithelia govern cell death and extrusion.
- Nature 544:212-216. Kawaguchi K, Kageyama R, Sano M (2017) Topological defects control collective
- dynamics in neural progenitor cell cultures. Nature 545:327-331. 30. Seč D. Čopar S. Žumer S (2014) Topological zoo of free-standing knots in confined
- chiral nematic fluids. Nat Commun 5:3057. 31. Martinez A, et al. (2014) Mutually tangled colloidal knots and induced defect loops
- in nematic fields. Nat Mater 13:258-263. 32. Wang X, Miller DS, Bukusoglu E, de Pablo JJ, Abbott NL (2016) Topological defects in liquid crystals as templates for molecular self-assembly. Nat Mater 15:106-112
- 33. Forster D, Lubensky TC, Martin PC, Swift J, Pershan PS (1971) Hydrodynamics of liquid crystals. Phys Rev Lett 26:1016.
- 34. de Gennes PG. Prost J (1995) The Physics of Liquid Crystals (Oxford Univ Press, Oxford).
- 35. Sengupta A, Herminghaus S, Bahr C (2014) Liquid crystal microfluidics: Surface, elastic and viscous interactions at microscales. Lig Cryst Rev 2:73-110.
- 36. Hernàndez-Navarro S, Tierno P, Farrera JA, Ignés-Mullol J, Sagués F (2014) Reconfigurable swarms of nematic colloids controlled by photoactivated surface patterns. Angew Chem Int Ed Engl 53:10696-10700.
- 37. Stark H (2001) Physics of colloidal dispersions in nematic liquid crystals. Phys Rep 351:387-474.

- 38. Henrich O, Stratford K, Coveney PV, Cates ME, Marenduzzo D (2013) Rheology of cubic blue phases. Soft Matter 9:10243-10256.
- Córdoba A, Stieger T, Mazza MG, Schoen M, de Pablo JJ (2016) Anisotropy and probe-medium interactions in the microrheology of nematic fluids. J Rheol 60:
- 40. Batista VMO, Blow ML, da Gama MMT (2015) The effect of anchoring on the nematic flow in channels. Soft Matter 11:4674-4685.
- Sengupta A. et al. (2013) Liquid crystal microfluidics for tunable flow shaping. Phys Rev Lett 110:048303.
- 42. Thampi SP, Golestanian R, Yeomans JM (2015) Driven active and passive nematics. Mol Phys 113:2656-2665
- Tiribocchi A. Henrich O. Lintuyuori JS. Marenduzzo D (2014) Switching hydrodynamics in liquid crystal devices: A simulation perspective. Soft Matter 10:4580-4592.
- Sengupta A, Bahr C, Herminghaus S (2013) Topological microfluidics for flexible micro-cargo concepts. Soft Matter 9:7251-7260.
- Na YJ, Yoon TY, Park S, Lee B, Lee SD (2010) Electrically programmable nematofluidics with a high level of selectivity in a hierarchically branched architecture. ChemPhysChem 11:101-104.
- 46. Cuennet JG, Vasdekis AE, Psaltis D (2013) Optofluidic-tunable color filters and spectroscopy based on liquid-crystal microflows. Lab Chip 13:2721-2726.
- 47. Liu Y, Cheng D, Lin IH, Abbott NL, Jiang H (2012) Microfluidic sensing devices employing in situ-formed liquid crystal thin film for detection of biochemical interactions. Lab Chip 12:3746-3753.
- 48. Oswald P, Pieranski P (2005) Nematic and Cholesteric Liquid Crystals: Concepts and Physical Properties Illustrated by Experiments (CRC, Boca Raton, FL).
- 49. Beris AN, Edwards BJ (1994) Thermodynamics of Flowing Systems with Internal Microstructure (Oxford Univ Press, Oxford).
- 50. Pieranski P, Godinho MH, Čopar S (2016) Persistent quasiplanar nematic texture: Its properties and topological defects. Phys Rev E 94:042706.
- 51. Kamien RD (2002) The geometry of soft materials: A primer. Rev Mod Phys 74:953-971
- 52. Sengupta A, Herminghaus S, Bahr C (2012) Opto-fluidic velocimetry using liquid crystal microfluidics. Appl Phys Lett 101:164101.
- Kawasaki K (1984) Topological defects and non-equilibrium. Prog Theor Phys 79:161-
- 54. Denniston C (1996) Disclination dynamics in nematic liquid crystals. Phys Rev B 54:6272-6275
- 55. Denniston C, Orlandini E, Yeomans J (2001) Lattice Boltzmann simulations of liquid crystal hydrodynamics. Phys Rev E 63:056702.
- 56. Sengupta A, Tkalec U, Bahr C (2011) Nematic textures in microfluidic environment. Soft Matter 7:6542–6549.
- 57. Nobili M, Durand G (1992) Disorientation-induced disordering at a nematic-liquidcrystal-solid interface. Phys Rev A 46:R6174-R6177
- 58. Succi S (2001) The Lattice Boltzmann Equation for Fluid Dynamics and Beyond (Clarendon, Oxford).
- 59. Raynik M. Žumer S (2009) Landau-de gennes modelling of nematic liquid crystal colloids. Lia Crvst 36:1201-1214.
- 60. Landau LD, Lifshitz EM Theory of Elasticity (Butterworth-Heinemann, Oxford), 3rd Ed.
- 61. Kleman M. Lavrentovich OD (2007) Soft Matter Physics: An Introduction (Springer, New York).
- Pieranski P, Čopar S, Godinho MH, Dazza M (2016) Hedgehogs in the dowser state. Eur Phys J E Soft Matter 39:121.
- 63. Pieranski P (2014) Generation of umbilics by Poiseuille flows. Eur Phys J E Soft Matter